A numerical study of vortex-induced drag of elastic swimmer models

Thomas Engels[a,b,*], Dmitry Kolomenskiy[c], Kai Schneider[a] and Jörn Sesterhenn[b]
[a] M2P2-CNRS, Aix-Marseille Université, Marseille, France
[b] ISTA Technische Universität Berlin, Germany
[c] McGill University, Montréal, Canada
[*] Corresponding author, electronic adress: thomas.engels@mailbox.tu-berlin.de

Abstract–We present numerical simulations of simplified models for swimming organisms or robots, which rely on chordwise flexible elastic plates. We focus on the tip vortices originating from three-dimensional effects due to the finite span. These are important effects when predicting the swimmer's cruising velocity, since they contribute significantly to the drag force. We first simulate rectangular swimmers and compare with a recent experimental study, before considering an expanding and a contracting shape, which is the originality of the present work. We find the cruising velocity of the contracting swimmer to be higher than the rectangular one, which in turn is higher than the expanding one. We provide evidence that this finding is due to the tip vortices interacting differently with the swimmer.

I. Introduction

Swimming organisms exploit bending waves to produce propulsive force, an effect which has been extensively studied. Predicting the cruising velocity, however, remains challenging, as the drag force has to be taken into account. In the present work, we numerically simulate simplified "swimmers", which consist of a chordwise flexible plate undergoing a driven pitching motion at the leading edge, immersed in a viscous incompressible fluid. The solid is actively coupled with the fluid, i.e. we deal with a fluid–structure interaction problem. The emphasis is placed on the longitudinal tip vortices, which result from the finite span, and their contribution to the drag force.

The total drag acting on these swimming organisms or robots can be decomposed in the contributions of the friction drag and the vortex induced drag. The former contribution has been relatively well explored. Theoretical studies have considered the laminar boundary layer, which is either compressed or stretched by the undulatory motion of the swimmer [4]. This effect is usually referred to as the "Lighthill boundary-layer thinning hypothesis". More recently, Ehrenstein et al. [1] employed high-quality numerical simulations using body-fitted meshes to quantify and verify this hypothesis.

The vortex induced drag, which may play a significant role, has only recently gained the attention of experimentalists. In the context of simplified mechanical swimming robots, Raspa et al. [5] established a basic model to explain the influence of the finite aspect ratio by the formation of trailing longitudinal tip-vortices.

The present numerical study is inspired by these experiments, and should be seen as complimentary approach, given the difficulty of experimentally measuring the instantaneous flow field appropriately.

In a first step, using rectangular swimmers, we will reproduce some experimental results and confirm the interpretation that the tip vortices play a major role in the drag force of the swimmer. In a second step, we move on and modify the swimmer's shape and find that a contracting form may be advantageous in terms of terminal cruising speed.

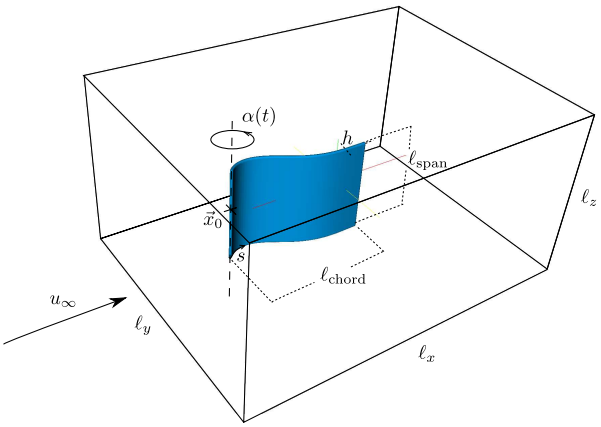

Figure 1: *Setup used in the present work. The swimmer, which consists of a spanwise flexible plate undergoing an imposed pitching motion $\alpha(t)$, is immersed in a viscous incompressible fluid with imposed mean flow $\vec{u}_\infty$.*

II. Materials and Methods

The experimental swimmer used in [5] consists of a Mylar sheet attached to a driving shaft, driven by a stepper motor. The whole swimmer, including the motor, is

allowed to move in the x-direction. It is immersed in a water tank. Experiments start with the swimmer at rest and observe the robot's accelerated motion. For the numerical simulations in the present work, some assumptions have to be made in order to reduce the problem's complexity sufficiently.

The numerical swimmer is assumed to be perfectly rigid in the spanwise and flexible only in the chordwise direction. Focusing on the chordwise flexibility greatly simplifies the complexity of the employed solid model—which can then be one-dimensional. Experimental findings show that spanwise deformations are present but rather small in magnitude, and taking them into account is left for future work. The swimmer is thus modeled as a slender beam, made of linearly elastic inextensible material, that undergoes large, non–linear deformations. The model is thus geometrically non–linear. The inextensibility condition, that is the conservation of the beam's length, can be treated by parametrizing the beam using the local deflection angle θ and the longitudinal internal force T. Together with the clamped-free boundary conditions, the governing equations for the solid read

$$\begin{aligned}\frac{\partial^2 T}{\partial s^2} - T\left(\frac{\partial \Theta}{\partial s}\right)^2 &= -2\eta\frac{\partial \Theta}{\partial s}\frac{\partial^3 \Theta}{\partial s^3} - \mu\left(\ddot{\Theta}+\ddot{\alpha}\right)^2 \\ &\quad -\eta\left(\frac{\partial^2 \Theta}{\partial s^2}\right)^2 - [p]^{\pm}\frac{\partial \Theta}{\partial s} \quad (1)\\ \mu\ddot{\Theta}+\mu\ddot{\alpha}+\frac{\partial [p]^{\pm}}{\partial s} &= -\eta\frac{\partial^4 \Theta}{\partial s^4} + 2\frac{\partial T}{\partial s}\frac{\partial \Theta}{\partial s} \\ &\quad +\left(T+\eta\left(\frac{\partial \Theta}{\partial s}\right)^2\right)\frac{\partial^2 \Theta}{\partial s^2} \quad (2)\end{aligned}$$

$$\left.\begin{aligned}\Theta &= 0\\ \frac{\partial T}{\partial s}+\eta\frac{\partial^2 \Theta}{\partial s^2}\frac{\partial \Theta}{\partial s} &= 0\\ T\frac{\partial \Theta}{\partial s}-\eta\frac{\partial^3 \Theta}{\partial s^3} &= [p]^{\pm}\end{aligned}\right\} \quad \text{at clamped end} \quad (3)$$

$$\left.\begin{aligned}T &= 0\\ \frac{\partial \Theta}{\partial s} &= 0\\ \frac{\partial^2 \Theta}{\partial s^2} &= 0\end{aligned}\right\} \quad \text{at free end} \quad (4)$$

Where α is the driven pitching motion, as illustrated in figure 1, $[p]^{\pm}$ is the pressure jump across the beam, s is the arclength coordinate and

$$\mu = \frac{h\rho_s}{\ell\rho_f} \qquad \eta = \frac{B}{\ell^3\rho_f U^2} \quad (5)$$

are the dimensionless density and stiffness, respectively. The material properties reported in [5] yield $\mu^{\text{exp}} = 0.0012$ and $\eta = 0.0134$. For numerical stability reasons, we set $\mu = 0.0096$ instead, as will be explained later. Two-dimensional simulations confirmed that the solution is not very sensitive to the value of μ in this regime. The swimmer's length $\ell_{\text{chord}} = 0.15$ [m], the fluid density $\rho_f = 1000\left[\text{kg/m}^3\right]$, a time scale $T = 1$ [s] and the velocity scale $U = \ell_{\text{chord}}/T$ have been used for normalization. The imposed pitching motion is sinusoidal, $\alpha = \alpha_{\max}\sin(2\pi f t)$ with $\alpha_{\max} = 50^\circ$. Contrary to the experiment, we do not vary the driving frequency f but keep it fixed at unity (thus $f = 1$ [Hz]).

The solid model equations (1-4) are solved using finite differences with an implicit time marching scheme, which treats all terms, including the non-linear ones, implicitly. Details about the solution procedure can be found in [2, 3].

The fluid is incompressible and Newtonian, and hence governed by the Navier–Stokes equations. To avoid using moving, body-fitted meshes, the flexible structure is taken into account using the volume penalization method. The governing penalized Navier–Stokes equations read

$$\begin{aligned}\partial_t \underline{u} + \underline{\omega}\times\underline{u} &= -\nabla q + \frac{1}{\text{Re}}\nabla^2\underline{u} - \frac{\chi}{\varepsilon}(\underline{u}-\underline{u}_s) \quad (6)\\ \nabla\cdot\underline{u} &= 0 \quad (7)\\ \underline{u}(\underline{x}, t=0) &= \underline{u}_0(\underline{x}). \quad (8)\end{aligned}$$

Note that eqns (6-8) do not contain no-slip boundary conditions, since the geometric information is encoded in the χ-function (where $\chi = 0$ in the fluid and $\chi = 1$ in the solid). The penalization parameter ε can be interpreted as solid permeability and is chosen to a very small value, $\varepsilon = 10^{-3}$ for example. Details about the penalization method for flexible obstacles can be found in [2, 3]. The mask function χ and the solid velocity field $\underline{u}_s$ are constructed from the solid model.

The numerical solution of eqns (6-8) is obtained in a periodic domain using a Fourier pseudospectral method and an explicit Adams-Bashforth type time stepping [6]. The grid is, due to the spatial discretization, uniform and equidistant. On the other hand no linear system has to be solved to impose the divergence-free constraint on the velocity field, which is a tremendous advantage and allows the code[1] to run on massively parallel supercomputers on $\mathcal{O}(10\,000)$ CPU.

Fluid-structure interaction problems are particularly challenging since two non-linear PDEs are coupled together, both yielding very different characteristics. The most important parameter for this coupling is the density ratio, which is defined by μ in the present article. The more similar the densities are, the more challenging the simulation. This can be explained by artificial added mass effects that destabilize simple coupling schemes, requiring the use of iterative algorithms. A short description using analytically handable toy models was presented by van Brummelen [7]. Since this work deals with swimming,

[1] Our code is open source and publicly available https://github.com/pseudospectators/FLUSI

performed in water, the simulations require an iterative coupling scheme. Still, as the number of iterations depends significantly on μ, we found that the experimental value $\mu^{\text{exp}} = 0.0012$ requires about 15-25 iterations (each at the price of one Navier–Stokes step), while the value we used, $\mu = 0.0096$, requires only 3-5. Two dimensional simulations confirm that the difference in results between both values is of a few per cent only, which justifies our choice of μ.

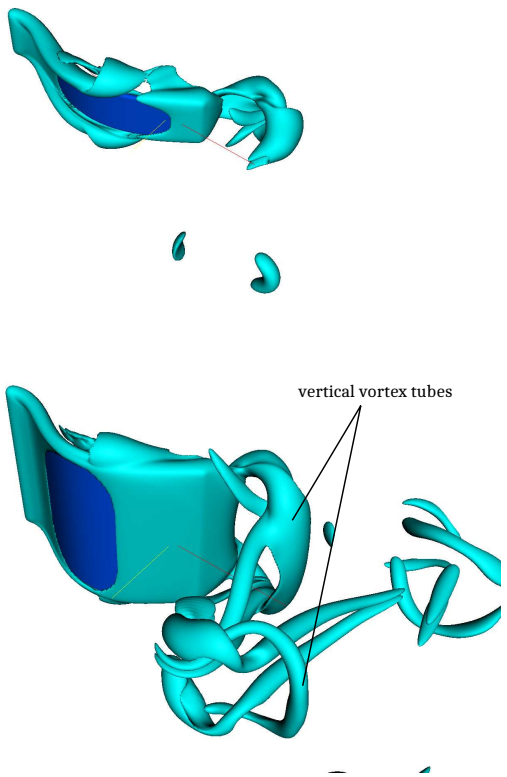

Figure 2: *Isosurfaces of vorticity* $\|\underline{\omega}\| = 17.5$ *for aspect ratios* $AR = 0.2$ *(top),* $AR = 0.7$ *(bottom). For* $AR = 0.2$*, the tip vortices dominate the flow*

IV. Rectangular Plates

In this section we present the results obtained for rectangular plates. The Reynolds number is $Re = U\ell_{\text{chord}}/\nu = 1000$, the swimmer is computed in a box of size $2.66 \times 2.00 \times 1.33$ wherein its leading edge at mid-span is located at $\underline{x}_0 = \begin{pmatrix} 0.5 & 1.0 & 0.66 \end{pmatrix}$. At this Reynolds number, we found a resolution of $512 \times 384 \times 256$ to be sufficient. The original experiment is performed at much higher Reynolds number of $Re = 22500$, which is currently out of scope for numerical simulations. The value of the penalization parameter is $\varepsilon = 10^{-3}$. The constant mean flow $\underline{u}_\infty = \begin{pmatrix} 0.5 & 0 & 0 \end{pmatrix}^T$ is impulsively started at $t = 0$ (thus the initial condition is $\underline{u}(\underline{x}, t = 0) = \underline{u}_\infty$), and we computed a total of 5 periods. Since our discretization is periodic, a vorticity sponge term is applied to all faces of the domain to prevent vortices from re-entering the domain, with a parameter of $\varepsilon_{\text{sp}} = 10^{-1}$, see [3] for more information about that boundary condition. During the first period, the imposed pitching angle is multiplied by a startup conditioner, i.e. $\alpha(t < 1) = \left(-20t^7 + 70t^6 - 84t^4 + 35t^4\right) \alpha_{\max} \sin(2\pi f t)$, in order to avoid an impulsively started motion, which would yield a pressure singularity. We carry out 4 simulations with varying aspect ratio, $AR = \ell_{\text{span}}/\ell_{\text{chord}} = \begin{Bmatrix} 0.2 & 0.3 & 0.5 & 0.7 & \infty \end{Bmatrix}$. The latter value corresponds to a 2D simulation, because the vortical structures are stable at Re=1000, which was verified by simulating a plate that extends periodically throughout the z-direction.

The vortical structure of the flow field is visualized in figure 2 for the smallest and largest value of AR, at the beginning of the fourth stroke $t = 4.05$. In the $AR = 0.7$ case, the vertical vortex tubes can be observed. These tubes correspond to the vortices shed in the 2D case, where $AR = \infty$. They connect to the tip vortices and form ring-like structures, propagating perpendicular to the mean flow which also advects them downstream. It is visible that, in the $AR = 0.2$ case, the tip vortices actually dominate the wake structure—the vertical vortex tubes are no clearly distinguishable.

The thrust force, that is the x-component of the hydrodynamic force, is shown in figure 3. Note that thrust points in negative x-direction. The solid line represents the prediction based on 2D simulations. The four 3D simulations are marked by circles. It can be observed that the thrust scales almost linearly with the aspect ratio. Assuming linearity, we make the ansatz

$$F_x^{3\text{D}} = F_{\text{thrust}} \cdot AR + F_{\text{tip}}$$

and fit the coefficients $F_{\text{thrust}} = -0.0628$ and $F_{\text{tip}} = 0.0165$ using least squares to the data points. In the case of 2D simulations, we found $F_x^{2\text{D}} = F_{\text{thrust}}^{2\text{D}} \cdot AR$ where the thrust per unit span is $F_{\text{thrust}}^{2\text{D}} = -0.0561$. We can thus observe that the values for the thrust per unit span are quite similar in both 3D and 2D cases, $F_{\text{thrust}} \approx F_{\text{thrust}}^{2\text{D}}$, and that the tip vortices indeed act like a constant offset. We can thus numerically confirm the experimental results presented by Raspa et al. [5].

V. Non-rectangular Shapes

The results for rectangular plates illustrate the importance of tip vortices for the total drag. Actual fish on the other hand have of course non-rectangular caudal fins, with possible consequences for the vortical structures in the wake. We choose an additional set of two different

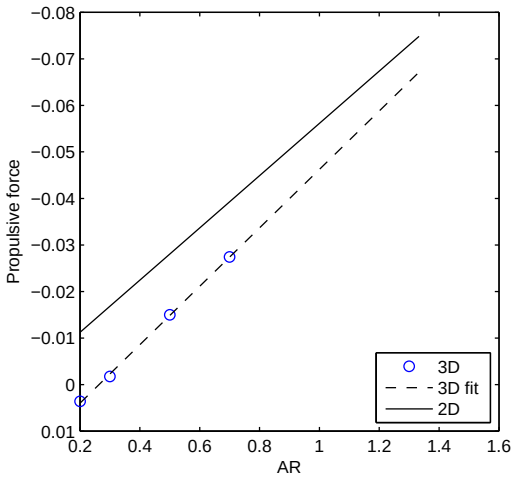

Figure 3: *Thrust force as a function of the aspect ratio. The solid line represents the force predicted by the 2D approximation and the dashed line is a linear least-squares fit through the available data points from the 3D simulations.*

shapes, an expanding and a contracting form, to study their influence on the cruising speed. All shapes have the same surface and follow the same imposed driving motion. For simplicity, we still assume the mechanical structure to be one-dimensional and with constant μ and η, although the varying $\ell_{\text{span}}(s)$ suggests that both should depend on s. This is a first order approximation, since both μ, η are linear in ℓ_{span}, but as $\eta \propto h^3$ the dominant effect of the stiffness η is captured and as μ is small anyways (light swimmer), this assumption seems justified. The non-rectangular shapes are defined as

$$\begin{aligned} \ell_{\text{span}}^{\text{exp}}(s) &= 2\left(\frac{0.35}{2} + 0.525s^2\right) \\ \ell_{\text{span}}^{\text{contr}}(s) &= 2\left(\frac{1.05}{2} - 0.525s^2\right) \end{aligned}$$

and are illustrated to scale in figure 4.

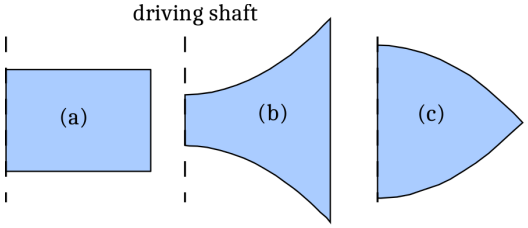

Figure 4: *Different shapes investigated here, termed (a) "rectangular", (b) "expanding" and (c) "contracting". All three shapes have the same surface.*

Since our swimmers remain anchored to the laboratory frame and instead move the surrounding fluid, it can be time-consuming to compute the steady state velocity, depending on the fluid domain size. In order to access the cruising speed, we instead solve the following ODE for the mean flow in x-direction:

$$\frac{\mathrm{d}}{\mathrm{d}t} u_\infty^{(x)} = \frac{\left\langle -\frac{\chi}{\varepsilon}\left(\underline{u} - \underline{u}_s\right)\right\rangle}{m_{\text{fluid}}}$$

where the initial condition is $u_\infty^{(x)}(t=0) = 0$. The mean flow is then set to $\underline{u}_\infty = \begin{pmatrix} u_\infty^{(x)} & 0 & 0 \end{pmatrix}^T$. The fluid mass to be accelerated is set to a relatively small value, $m_{\text{fluid}} = 0.1235$, in order to speed up the computation because the steady state is reached sooner than with larger values. Without modification, the fluid mass would be equal to the volume of the computational domain, $\ell_x \ell_y \ell_z = 7.07$. Figure 5 illustrates the result obtained for all swimmers. They all reach their steady state (to a good approximation) within 10 strokes, but the resulting cruising speed significantly depends on the swimmer's shape. The contracting shape ($\left\langle u_\infty^{(x)} \right\rangle = 0.75$) outruns both the rectangular ($\left\langle u_\infty^{(x)} \right\rangle = 0.70$) and the expanding ($\left\langle u_\infty^{(x)} \right\rangle = 0.55$) shapes.

One remarkable difference between the three simulations is that the expanding one has the smallest trailing edge displacement, which is due to the larger concentration of area there. The pressure acting on the tail is thus much higher in that case, reducing the deflection amplitude.

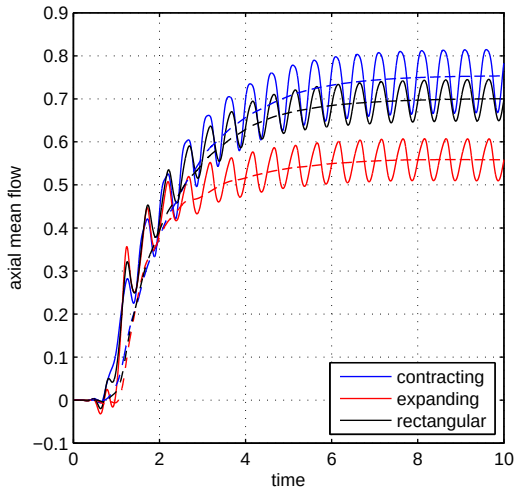

Figure 5: *Axial mean flow over time for the three different swimmers from figure 4. Solid lines is instantaneous data, dashed lines is a moving average over the duration of one stroke.*

All swimmers have finite span and thus exhibit tip vortices, and again these vortices offer a potential explanation

for the higher cruising velocity of the contracting shape. *A priori*, one might think the expanding form is advantageous, since the larger trailing edge will produce larger vertical tube vortices (cf figure 2), and thus reduce the spurious three-dimensional effects.

However, the opposite is true. Figure 6 shows the vortical structures for the contracting and expanding shape at the same time, which is during the steady cruising state. The tip vortices, shed in both configurations around mid-chord, are advected downstream due to the mean flow, and they can be associated with a zone of lower pressure. This drop in pressure creates a local net force pointing in the direction of the vortex core, and part of which contributes to the total drag force (depending on the orientation of the surface normal relative to the x-direction). Visibly, in the contracting case, the tip vortex quickly looses contact with the actual swimmer – it's parasitic drag is thereby reduced. The opposite is true for the expanding type swimmer: not only does the tip vortex not loose contact with the swimmer, it does instead even increase the portion of the swimmer influenced by the tip vortices, compared to the rectangular swimmer. It can also be noted that the total mean enstrophy,

$$\langle Z \rangle = \left\langle \iiint \|\underline{\omega}\|^2 \, d\underline{x} \right\rangle,$$

which is a measure for the dissipation in the fluid wake, is significantly higher in the expanding than in the contracting case, $\langle Z \rangle_{\text{contracting}} = 98.7$ versus $\langle Z \rangle_{\text{expanding}} = 127.7$, indicating a higher dissipation rate in the expanding case.

VI. Conclusion

We numerically simulated the flow past simplified elastic swimmer models. These models consist of flexible plates that have a driven pitching angle at their leading edges. In the first part, we simulated rectangular swimmers, that are inspired by the experimental work presented in [5]. We confirmed the finding that the tip vortices are a significant contribution to the total drag, and thus should be taken into account when predicting the cruising speed of these swimmers. We showed that indeed the 3D nature of these flows acts like a parasitic drag that is virtually independent of the aspect ratio.

In a second step, with the insight gained in the first one, we investigated shapes other than rectangular, namely a contracting and an expanding one, and compared their cruising velocities. We found that the contracting shape is the best, and postulate that this may possibly be explained by the tip vortices quickly "loosing touch" to the swimmer, which reduces their influence on the drag.

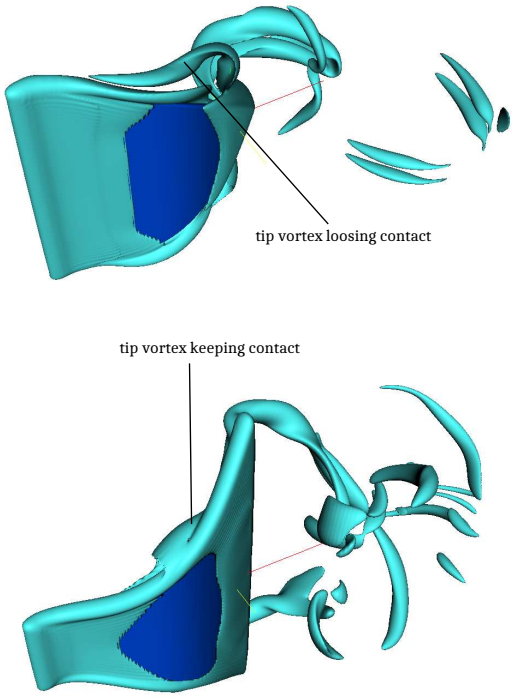

Figure 6: *Isosurfaces of vorticity* $\|\underline{\omega}\| = 17.5$ *for contacting (top) and expanding shapes (bottom).*

References

[1] U. Ehrenstein, M. Marquillie, and C. Eloy. Skin friction on a flapping plate in uniform flow. *Phil. Trans. R. Soc. A*, 372, 2014.

[2] T. Engels, D. Kolomenskiy, K. Schneider, and J. Sesterhenn. Two-dimensional simulation of the fluttering instability using a pseudospectral method with volume penalization. *Computers & Structures*, 122:101–112, 2012.

[3] T. Engels, D. Kolomenskiy, K. Schneider, and J. Sesterhenn. Numerical simulation of fluid-structure interaction with the volume penalization method. *J. Comput. Phys.*, 2014, under revision.

[4] M. J. Lighthill. Large-amplitude elongated-body theory of fish locomotion. *Proc. R. Soc. Lond. B*, 179:125–138, 1971.

[5] V. Raspa, S. Ramananarivo, B. Thiria, and R. Godoy-Diana. Vortex-induced drag and the role of aspect ratio in undulatory swimmers. *Phys. Fluids*, 26(4), 2014.

[6] Kai Schneider. Numerical simulation of the transient flow behaviour in chemical reactors using a penali-

sation method. *Computers & Fluids*, 34:1223–1238, 2005.

[7] E. H. van Brummelen. Added mass effects of compressible and incompressible flows in fluid-structure interaction. *J. Appl. Mech.*, 76:021206, 2009.